



Mathematical model for silicon electrode – Part II. Simulations on different electrode nanostructures



Sumitava De^a, Joseph Gordon^b, Godfrey Sikha^{b,*}

^a Department of Energy, Environmental and Chemical Engineering, Washington University, St. Louis, MO 63130, USA

^b Applied Materials Inc., 3225 Oakmead Village Drive, Santa Clara, CA 95054, USA

H I G H L I G H T S

- 1-d axisymmetric plane strain model to study stress in different Si nanostructures.
- 1-d model is a dimensionally reduced form of the 2-d model presented in part I.
- 1-d and 2-d model results compare well for the Si nanowire.
- Si nanotubes expected to perform better in terms of mechanical stability.
- Carbon-Si core/shell structures exhibit high stress generation at interface.

A R T I C L E I N F O

Article history:

Received 17 February 2014

Accepted 26 March 2014

Available online 15 April 2014

Keywords:

Li-ion batteries

Silicon anodes

Intercalation induced stresses

Mathematical model

A B S T R A C T

The second part of the manuscript presents a one-dimensional axisymmetric plane strain model to study lithium insertion induced stresses in different types of silicon nanostructures, – nanowire (Si NW), nanotube (Si NT) and core/shell (Si C/S) nanostructures. The 1-d plane strain model is the dimensionally reduced form of the 2-d model presented in part I. Simulation results from the 1-d plane strain model is compared to the results from the 2-d model for the Si NW. Each of these structures poses a different type of boundary conditions and the stress evolution due to diffusion in each of the cases are discussed. Simulation results indicate that Si NT structures develop lower tensile stresses compared to Si NW structures under similar current densities. Case studies on Si NT for different values of inner to outer radii ratio are also presented. Furthermore, simulations reveal that the Si C/S structures develop much higher stresses (closer to the core/shell interface) compared to Si NW or Si NT, owing to the different expansion factors of the core and shell material.

© 2014 Elsevier B.V. All rights reserved.

1. Introduction

Nanostructured electrodes have been proposed to alleviate the detrimental effects of large volume changes due to lithium insertion in Si electrodes. Experiments have demonstrated that nanostructured materials [1–3] can better accommodate large diffusion induced stresses caused due to insertion and de-insertion of lithium, thereby increasing cyclability of Si electrodes. Many research groups have reported the use of various nano-structured materials including Si nanowires, Si nanotubes, core–shell Si

nanowires etc. as electrodes in lithium-ion batteries in an attempt to increase cycle life and performance of the materials [1–6]. Yao et al. [7] reported interconnected Si hollow nanospheres as Li-ion battery anodes with high cycle life as a result of reduced stresses due to the hollow space compared to solid structures. Song et al. [4] shows similar reduction of stress in Si NT. Liu et al. [8] reported a yolk–shell structure consisting of Si nanoparticle enclosed in a carbon shell with void space between particle and shell so that particle can expand freely during lithiation without breaking the shell. Core shell (carbon/Si) nanostructures have also been reported in literature for use as high capacity anodes for Li ion batteries [3,9]. The authors claim that the carbon core provides mechanical support to the nanostructure system making it more stable when huge stresses build up during lithiation. Other novel structures have been reported in literature to better accommodate volume expansion in silicon, such as a carbon–aluminum–silicon nanostructure

DOI of original article: <http://dx.doi.org/10.1016/j.jpowsour.2014.03.022>.

* Corresponding author.

E-mail addresses: Godfrey_Sikha@amat.com, Sikha.Godfrey@gmail.com (G. Sikha).

comprising of a carbon nanorod, a sandwiched layer of aluminum, capped by a nanoscoop of silicon, [10] which exploits the graded strain properties of the three different materials to accommodate the volume expansion during lithiation. In an earlier work (Part I of this paper), we presented a 2-d model for electrochemical lithiation of a Si nanowire. In this article, we present a simplified, 1-dimensional, computationally efficient mathematical model to simulate stress generation, volume expansion etc. due to lithium insertion. The 1-d model is used to simulate lithiation of the following silicon based nano-structured electrodes, – nanowire (Si NW), nanotube (Si NT) and core/shell (Si C/S) nanostructures.

2. Model development

A detailed transient axisymmetric two dimensional model (2-d model) to simulate the electrochemical lithium insertion in Si nanowire has been developed in part I of the paper. The 2-d model was reduced to a 1-d model in r co-ordinate with the intent of minimizing computational run time which facilitates faster analysis of multiple structures. The key assumptions which are similar for both 1-d and 2-d models were discussed in part I. Additional assumptions involved in the 1-d model are as follows:

- The total strain in the axial z direction (ϵ_{zz}) is assumed to be zero since the axial dimension of each nanostructure is much greater compared to the radius. This assumption neglects the variation of all variables including the displacement due to lithium insertion in the z direction facilitating the development of a one dimensional axisymmetric plane strain model. The 1-d plane strain model is expected to be representative in regions away from the top and bottom edges of the nanostructures.
- Transport of Li in Si host due to diffusion, pressure gradient and bulk transport is considered only in the radial direction and transport in the axial and tangential co-ordinates is ignored.
- The current collector constraint at the base of nanostructure is ignored which is also representative of region far away from the top and bottom of the nanostructures.
- For the Si NT, the inner surface is assumed to be devoid of electrolyte, thereby ignoring any electrochemical reaction.
- For the Si shell carbon core structures, lithium insertion in the carbon core is neglected, due to relatively smaller volume element and lower expansion of carbon compared to Si.

The paper presents a study and analysis of stress distributions for different silicon based nanostructured electrodes using the simplified 1-d model. The different nanostructures considered are a) Silicon nanowire (Si NW) b) Silicon nanotube (Si NT) c) Silicon

shell carbon core (Si C/S) nanostructures. Fig. 1 shows the schematic of the structures. The 1-d model is treated with necessary modifications for each nanostructure along with appropriate boundary conditions to simulate each case. The results from 1-d Si-NW model are compared to those from the 2-d model.

2.1. Model equations

2.1.1. Material balance

The material balance equations related to the 1-d model are similar to those described in part I of paper. An exception is that for the 1-d model, axial variation is neglected and quantities vary only across r . Therefore using similar notations as in part I of the paper, the flux of lithiated host or species LiS is expressed as follows:

$$N_{\text{LiS}} = x_{\text{LiS}}(N_{\text{LiS}} + N_{\text{S}}) - c_{\text{T}}D_{\text{LiS,S}} \left[\alpha_{\text{LiS}} \frac{\partial x_{\text{LiS}}}{\partial r} + \frac{x_{\text{LiS}}}{RT} \left(\bar{V}_{\text{LiS}} - \frac{M_{\text{LiS}}}{\rho} \right) \frac{\partial p}{\partial r} \right] \quad (1)$$

The material balance for species LiS is given by

$$\frac{\partial c_{\text{T}}x_{\text{LiS}}}{\partial t} + \frac{1}{r} \frac{\partial}{\partial r} (rN_{\text{LiS}}) = 0 \quad (2)$$

2.1.2. Solid mechanics

Due to the plane strain assumption, the axial strain is taken to be zero i.e. $\epsilon_{zz} = 0$. Therefore, the large deformation strain matrix is reduced to the following equation for the 1-d case:

$$\epsilon = \begin{bmatrix} \epsilon_{rr} & \epsilon_{r\theta} & \epsilon_{rz} \\ \epsilon_{\theta r} & \epsilon_{\theta\theta} & \epsilon_{\theta z} \\ \epsilon_{zr} & \epsilon_{z\theta} & \epsilon_{zz} \end{bmatrix} = \begin{bmatrix} \frac{\partial u}{\partial r} + \frac{1}{2} \left(\frac{\partial u}{\partial r} \right)^2 & 0 & 0 \\ 0 & \frac{u}{r} + \frac{1}{2} \left(\frac{u}{r} \right)^2 & 0 \\ 0 & 0 & 0 \end{bmatrix} \quad (3)$$

Here u is the radial displacement corresponding to elastic strain. The radial and tangential stresses are related to the strain using linear Hooke's Law given by

$$\tau = \lambda \text{tr}(\epsilon)(\mathbf{I}) + 2\mu(\epsilon) \quad (4)$$

where τ is the stress tensor, λ and μ being the Lamé constants. The corresponding equilibrium force balance equation reduces to

$$\frac{\partial \sigma_{rr}}{\partial r} + \frac{\sigma_{rr} - \sigma_{\theta\theta}}{r} = 0 \quad (5)$$

The respective one dimensional force and material balances were solved in a similar procedure discussed in part I for the Si NW, Si NT and Si shell (for core shell structures) domains. For the Si shell carbon core structures, the model variables were also solved inside the carbon core domain. The equilibrium force balance equation (Eq. (5)) is valid in the core domain. As per our assumption, there is no Li insertion into the core, so the total strain, ϵ_{T} is purely elastic and the chemical strain component is absent in the core. Therefore the radial displacement component u is the only variable to be solved for in the core domain.

2.2. Boundary and initial conditions for different nanostructures

2.2.1. Case A. Silicon nanowire

The 1-d model is solved for a constant current case. It should be noted that the outer radius specified by R_0 changes with time as the

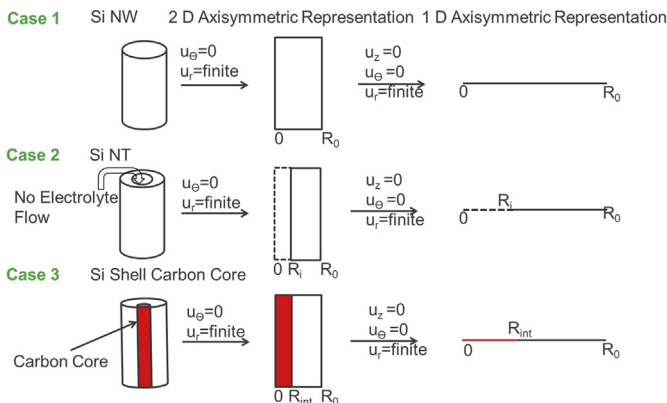


Fig. 1. Schematic and modeling geometry representation of Si based nanostructures considered for model development.

structure expands during lithiation. At the outer surface, the current flux boundary condition for constant current condition is applied.

$$-n \cdot N_{\text{LiS}}|_{r=0} = \frac{-S_i i_{\text{app}}(t)}{F} \quad (6)$$

i_{app} represents the current density which is a function of time due to the changing outer surface area. The applied current is constant which satisfies the galvanostatic conditions. The axial symmetry condition is used at center of the wire for simulation. The outer surface of the Si NW is assumed to be a free surface, therefore the appropriate boundary condition for stress is

$$-n \cdot \tau|_{r=R_0} = 0 \quad (7)$$

At the center of the Si NW, a symmetry boundary condition is maintained for stress.

2.2.2. Case B. Silicon nanotube

For the Si NT both the internal and external radii defined as R_0 and R_i respectively are functions of time as the structure expands due to lithiation. As the inner surface of the nanotube is assumed to be devoid of electrolyte, any electrochemical reactions at the inner interface can be ignored and therefore a zero flux condition is used. At the outer surface, a constant current flux condition is used. Therefore, the appropriate boundary conditions are given by:

$$n \cdot N_{\text{LiS}}|_{r=R_i} = 0 \quad (8)$$

$$-n \cdot N_{\text{LiS}}|_{r=R_0} = \frac{-S_i i_{\text{app}}(t)}{F} \quad (9)$$

For the Si NT, both the inner and outer surfaces are assumed to be free surfaces, therefore the proper boundary conditions are as follows:

$$-n \cdot \tau|_{r=R_i} = 0 \quad (10)$$

$$-n \cdot \tau|_{r=R_0} = 0 \quad (11)$$

2.2.3. Case C. Si shell carbon core structures

For the core–shell structures, there are two distinct domains, inner region representing the carbon core and the outer region representing the Si shell. The interface between the core and shell is represented by R_{int} which changes position with time. As mentioned earlier, we assume that lithium insertion inside the carbon core is ignored. It should be noted that in practical applications, there is a range of potentials in which C and Si can co-insert lithium. However, for the structures used in the simulations, the ratio of the volume of carbon to Si is small (1/81), and furthermore, carbon does not undergo significant volume expansion ($\sim 8\%$) compared to Si. Therefore, ignoring lithium insertion in carbon structures is a reasonable assumption. The model could also be applicable to similar shell core structures [3]. A constant current condition is assumed for the outer surface of the shell. Therefore, the correct boundary conditions for outer surface of Si shell and core/shell interface are as follows respectively:

$$-n \cdot N_{\text{LiS}}|_{r=R_0} = \frac{-S_i i_{\text{app}}(t)}{F} \quad (12)$$

$$-n \cdot N_{\text{LiS}}|_{r=R_{\text{int}}} = 0 \quad (13)$$

The outer surface of the core–shell structure is assumed to be a free surface without constraints, therefore the appropriate boundary condition is

$$-n \cdot \tau|_{r=R_0} = 0 \quad (14)$$

At the core–shell interface, the radial stresses and displacements are taken to be continuous. At the center of the core, symmetry conditions are maintained.

2.2.4. Initial conditions

The appropriate initial conditions required for simulating all three case studies are:

$$u|_{t=0} = 0 \quad (15)$$

$$x_{\text{LiS}}|_{t=0} = 0 \quad (16)$$

3. Solving methodology & parameters

The model was developed and executed in COMSOL Multiphysics. The force balance equation (Eq. (5)) was solved in all domains using the in-built structural mechanics module. The material balance equation (Eq. (2)) was incorporated in a general PDE interface to solve in the respective domains. The 1-d problem was developed by invoking the 2-d axisymmetric geometry module in COMSOL Multiphysics and imposing the zero flux condition for all variables solved for along the axial coordinates. As mentioned in Part I of the paper, the deformation of the mesh is calculated directly from the total displacement components (elastic and chemical strains) which are calculated from structural mechanics module, therefore making it a Lagrangian method. The Arbitrary Lagrangian–Eulerian method was employed as the mesh movement technique. The parameters used for simulation are given in Table 1. The outer surface flux boundary condition has the current density $i_{\text{app}}(t)$ which is calculated based on the ratio of total applied current and the varying outer surface area. The flux at the outer surface is related to the current density through Eq. (6). For the Si shell carbon core case, as no lithium insertion is assumed inside the CNT core, the total current is calculated based on the initial volume of the Si shell only. For the Si NT, the initial volume of the annular portion

Table 1

List of parameter values used in the simulation.

Parameter	Value	Units
Diffusion coefficient of Li in Si, D_{LiS} [20]	2×10^{-12}	$\text{cm}^2 \text{s}^{-1}$
Maximum number of moles of Li that can reversibly alloy per mole of Si, Δx	15/4	No units
Maximum insertion coefficient of Li in LiS, Δz_{max}	1	No units
Thermodynamic factor, α_{LiS}	1	No units
Partial molar volume of Li in Si, \bar{V}_{LiS}	13.1	ml mol^{-1}
Young's modulus, E [21,13]	92.16 (for LiS, 200 (for SWCNT), 30 (for MWCNT))	GPa
Poisson's ratio, ν	0.27 (for LiS), 0.35 (for SWCNT & MWCNT)	No units

was considered for total current calculation. Single walled and multi walled carbon nanotubes were considered as core materials for Si shell carbon core structures which were simulated with appropriate parameters. These cases henceforth will be addressed as SWCNT/Si and MWCNT/Si respectively.

4. Results and discussion

In this section, simulation results from the 2-d model (presented in part I) and 1-d model (presented here) are compared. Subsequently, simulation results for other nanostructures are discussed. The stress evolution in different type of nano-structures is also discussed.

4.1. Electrochemical lithiation of silicon nanowire (Si NW)-1-d vs 2-d model

As stated earlier, the 1-d axisymmetric plane strain model was developed by invoking a 2-d axisymmetric geometry in COMSOL and imposing zero flux conditions along the axial co-ordinate which renders the 1-d model valid only far away from the top and base of the 2D geometry. To compare the results from the 1-d model to the 2-d model (developed in part I of the paper), variables were evaluated at a radial cut at half the height of the chosen 2-d axisymmetric geometry i.e., for the 2-d model the stress profiles were obtained across radius at height of $z = H_{Cu} + H_{NW}/2$ and were compared with the results from the 1-d model. Fig. 2 presents the comparison of radial and tangential stress profiles obtained from 1-d and 2-d models at times $t = 1, 10, 100$ and 1000 s. The 1-d model was used to simulate the electrochemical lithiation of Si NW of radius 50 nm and height 10μ at $1C$ rate. From the figure, it is evident that the stress profiles from

both the 1-d and 2-d models agree well qualitatively. Both models predict the increase in stress at start of lithiation and the subsequent decrease over a broad time scale on continuous lithiation. The tensile nature of the tangential and radial stress components towards the center and equality of radial and tangential stress at the center of the wire are accurately captured by both the models. The compressive nature of the tangential stress at the surface of the nanowire is also captured by both the models. At longer times, the value of radial and tangential stresses obtained from the 1-d model are observed to be higher in magnitude than the 2D model. ($\sim 25\%$ difference in radial and tangential stresses at the center and $\sim 25\%$ difference in tangential stresses at the outer surface). This is possibly due to the negligence of the current collector base in the 1-d model. Also, the 1-d plane strain model ignores the effect of axial strain, which can impact the radial and the tangential components. It is worth noting that the axial stresses dominate at longer times (see part I), which can be the reason for the increased deviation observed between 1-d & 2-d models at longer times. The deviation in stress profiles also lead to differences in prediction of expanded radius (at the end of lithiation). The increased radial stresses observed for the 1-d model at longer times, results in higher predictions of the expanded radius. There is $\sim 3.7\%$ difference in prediction of the expanded radius between the 1-d and 2-d models.

Fig. 3 shows the maximum radial and tangential stress profiles predicted by the 1-d and 2-d models. The structure simulated is Si NW of radius 50 nm and height 10μ at $1C$ rate. The maximum radial and tangential stresses always occur at the center and outer surface of Si NW respectively. The qualitative features of the maximum stress profiles e.g. the increase and decrease of stresses with time and occurrence of peak stresses are in good agreement between the 1-d and 2-d models. The maximum radial & tangential stresses are

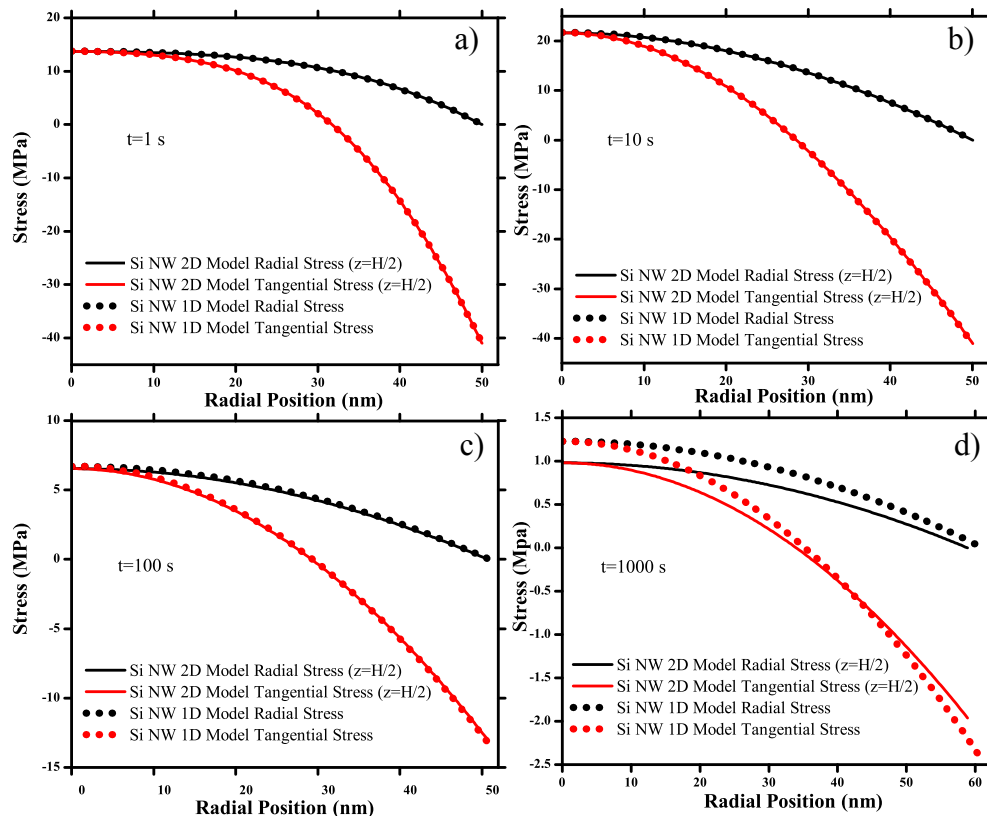


Fig. 2. Comparison of radial and tangential stresses for 1-d and 2-d models for Si-NW at times: a) 1 s b) 10 s c) 100 s d) 1000 s.

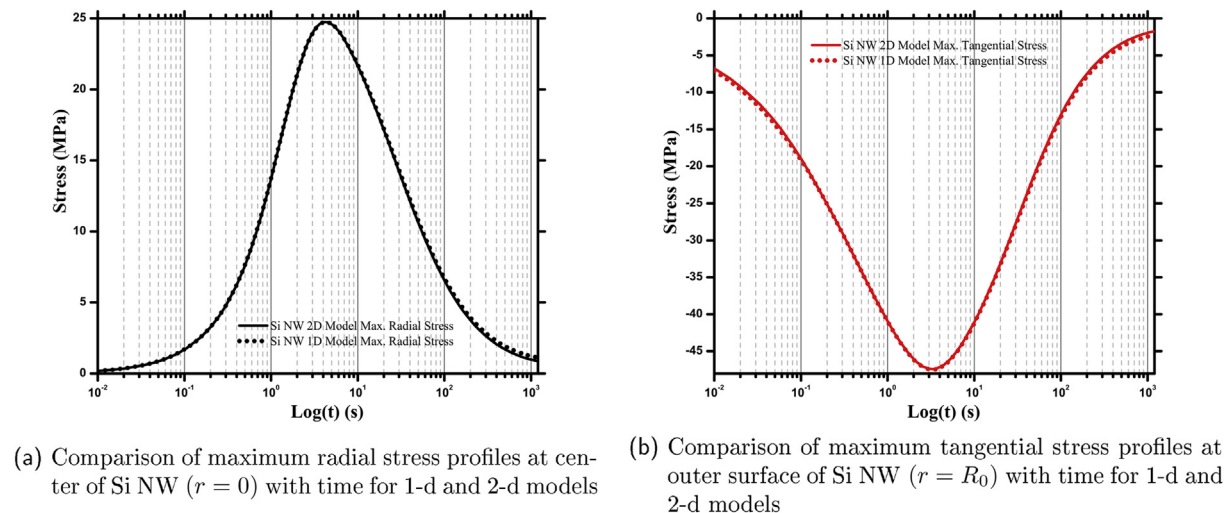


Fig. 3. Plots comparing evolution of maximum radial and tangential stress profiles with time for Si NW from 1-d and 2-d models.

also in good quantitative agreement, except at longer times, i.e., towards end of lithiation. The possible reason for this difference was explained earlier.

Fig. 4a and b compares the maximum radial and tangential stresses obtained from the 1-d and 2-d models as a function of the rate of lithiation (C rate) of Si NW of radius 50 nm and height 10 μ m. The C rates chosen were C/10, C/2, C, 2C and 5C. Most of the general features such as the increase and decrease of stresses with time, increase in peak stresses and shift of peak stresses towards shorter times with increasing rates are qualitatively in good agreement between both the 1-d and 2-d models. The difference in the radial and tangential stress predictions from the models increases with increase in charging rate towards the end of lithiation (radial stress $\sim 1\%$ difference & tangential stress $\sim 1\%$ difference at 1C rate vs. radial stress $\sim 11\%$ difference at 5C rate, and tangential stress $\sim 11\%$ difference at 5C rate at $t = 100$ s). This observation can be explained as an effect of negligence of base and axial strain in the 1-d model as mentioned previously. Furthermore, the tangential stresses predicted by the 1D model is higher than the 2-d model, at short

times, especially at higher rates (68% at 1C rate vs. 70% at 5C rate at $t = 2$ ms). Overall, as the predictions from the 1-d model compare quite well to those from the 2-d model, therefore, it was used to study other nanostructures.

4.2. Silicon nanotube (Si NT)

To simulate nanotube structures, a Si NT structure with an outer radius of 50 nm and an inner to outer radius i.e., R_i/R_0 of 0.1 was considered. The simulation results from the Si NT structure were compared to the results from Si NW (50 nm radius) for lithiation at 1C rate. Fig. 5 compares the radial stress profiles for Si NW to Si NT at times 1, 10 and 100 s respectively. From the plots it is evident that for the Si NT, the stresses are tensile along the radius and tend towards zero at the inner and outer edges as a result of free surfaces. Similar to Si NW, the stresses in the Si NT increase at short times with initial lithiation (< 10 s), and decrease at longer times (> 10 s) towards the end of lithiation. For the Si NW, the maximum radial stress always occurs at the center, whereas for the Si NT, the

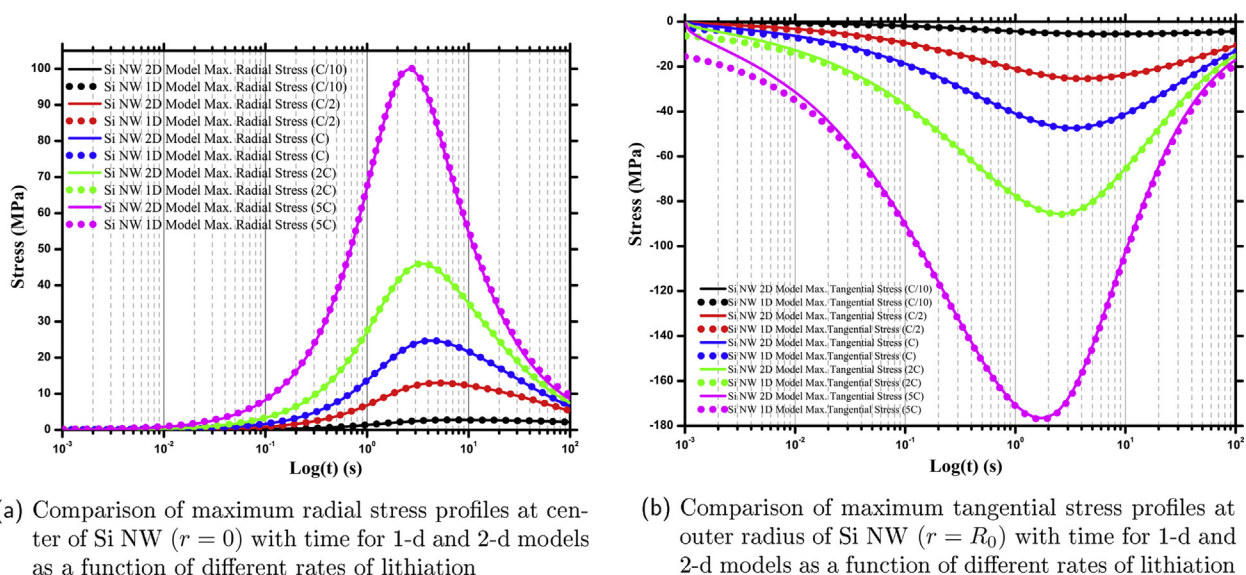


Fig. 4. Plots comparing evolution of maximum radial and tangential stress profiles of Si NW with time for 1-d and 2-d models as a function of different rates of lithiation.

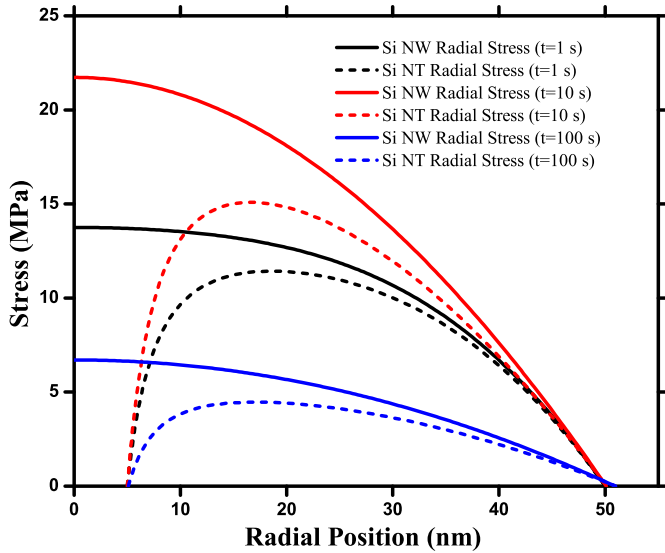


Fig. 5. Comparison of radial stress profiles for Si NW and Si NT at various times $t = 1, 10$ and 100 s.

maximum radial stress occurs somewhere along the radius as a function of time and moves closer to the inner radius with increasing time. Also, the local radial stresses developed across the radius in the Si NT is in general lower than that of the stresses in the NW. A comparison of maximum radial stress profiles of Si NW and Si NT with time is presented in Fig. 6. Furthermore, Fig. 5 also shows that lithiation of the Si NT causes the inner interface to move away from the initial position (not obvious from the plot in Fig. 5). At $t = 100$ s, the inner surface has a positive displacement of about 0.102 nm from its initial position.

Fig. 7 compares the tangential stress profiles across the radius of the Si NW and Si NT at times 1, 10 and 100 s. The tangential stresses in Si NT are tensile at the inner surface and compressive at the outer surface, similar to the behavior of Si NW. The tangential stress in Si NT structure is higher in magnitude closer to the inner radius compared to the tangential stress at center of the Si NW. In fact, at the interface, the Si NT tangential stress is significantly higher than

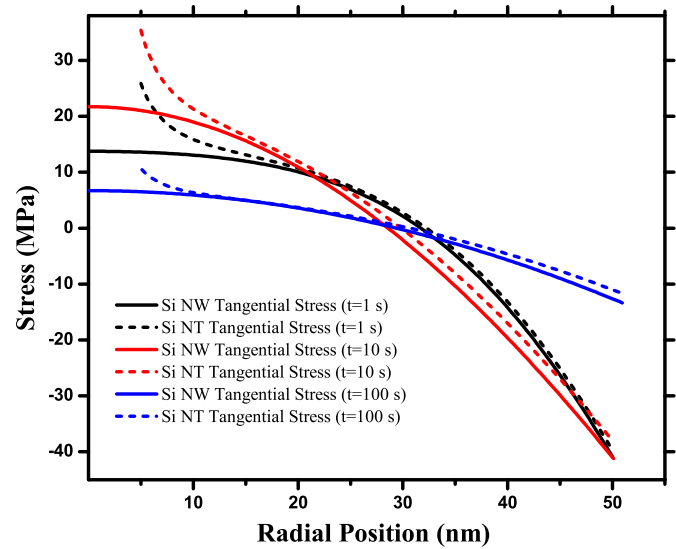


Fig. 7. Comparison of tangential stress profiles for Si NW and Si NT at various times $t = 1, 10$ and 100 s.

the Si NW center tangential stress, however closer to the surface, the Si NT tangential stress is lower in magnitude compared to the Si NW.

The 1-d model was used to study the effect of R_i/R_0 i.e., inner to outer radius ratio on the radial stress profiles for the Si NT of fixed initial outer radius of 50 nm for 1C rate. The radius ratios considered were 0.05, 0.1, 0.2, 0.3 and 0.4, which correspond to volume ratios (void volume to Si volume) of 0.0025, 0.01, 0.042, 0.099 and 0.19 respectively. The radial stresses at $t = 10$ s are shown in Fig. 8. For each case, the local radial stresses developed across the radius in the Si NT are lower in magnitude for larger radius ratios. Furthermore, the peak radial stress shifts away from the inner surface for Si NT structures with larger radius ratios.

Based on the simulation results of the Si NT, the radial stresses are lower compared to the Si NW, while the tangential stresses (interface and regions close to interface) are higher in Si NT compared to Si NW. Also, the radial stresses are lower in magnitude

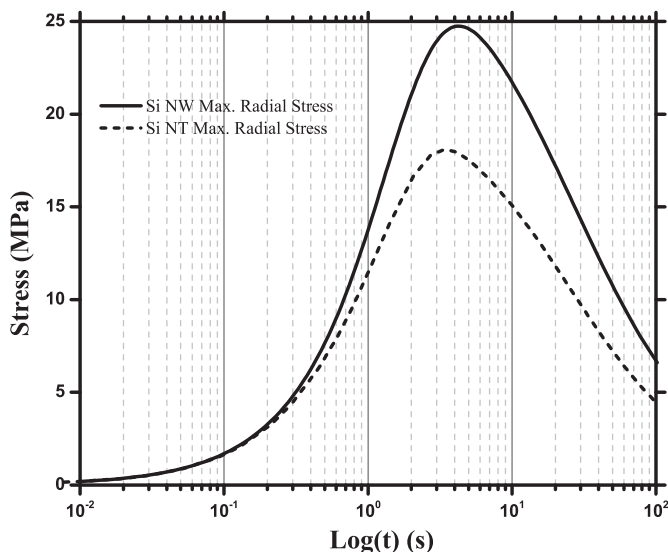


Fig. 6. Comparison of maximum radial stress profiles for Si NW and Si NT with time.

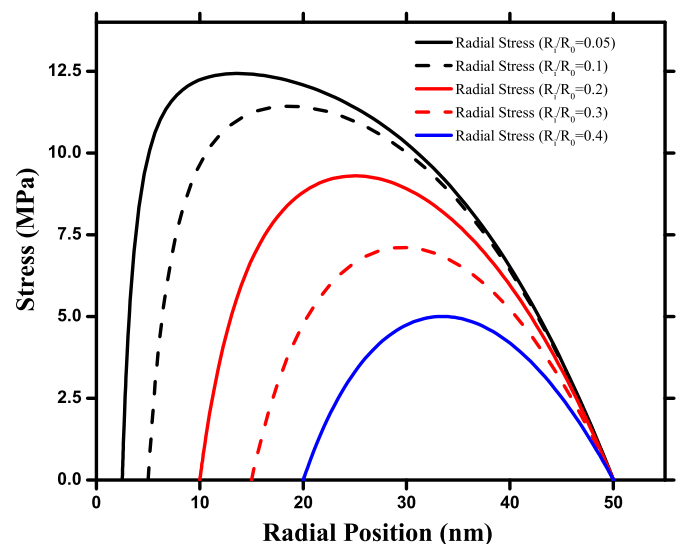


Fig. 8. Comparison of radial stress profiles for Si NTs of inner to outer radius ratio $R_i/R_0 = 0.05, 0.1, 0.2, 0.3$ and 0.4 at time $t = 10$ s.

for increasing R_i/R_0 values for Si NT. Consequently, more simulation runs were performed to compare radial and tangential stresses of Si NT to Si NW for various R_i/R_0 values. Fig. 9 shows the magnitudes of maximum tensile stresses for the Si NT for different R_i/R_0 ratios. The initial outer radius for both NW and NT was 50 nm. For the Si NT, the tangential component of the maximum tensile stress occurs at the inner surface while the maximum radial stress component occurs somewhere along the radius. The maximum tensile stress for the Si NW always occurs at the center where the radial and tangential stresses are equal in magnitude. As mentioned earlier, the radial component of the tensile stress decreases with increasing inner to outer radius ratios for the Si NT. Interestingly, the tangential component of the maximum tensile stress also follows a similar trend. For the case when the radius ratio becomes zero i.e., $R_i/R_0 = 0$ which represents Si NW, the radial and tangential components of the maximum tensile stress become equal as a result of the symmetry boundary condition represented by the solid horizontal line. In general, although the radial component of the maximum tensile stress are always smaller in the case of Si NT compared to Si NW, the tangential component is larger than that of Si NW. This scenario reverses for radius ratio values greater than 0.4, where both the radial and tangential components of maximum tensile stresses for Si NT are smaller than Si NW. Such a design is beneficial to minimize the overall stress induced in nano-structure. However, increase in the hollow space for the Si NT of fixed initial outer radius decreases the charge capacity. For a radius ratio of 0.4, the volumetric capacity of Si NT decreases by 16% compared to Si NW.

4.3. Silicon shell carbon core structure

The 1-d model was also used to study core–shell structures. Use of core–shell carbon/Si nanostructures for anodes for use as negative electrodes in lithium-ion batteries have been reported in literature [11,12,9]. Cui and co-workers [12] reported synthesis of amorphous silicon using chemical vapor deposition technique onto carbon nano-fibers, casted on stainless steel substrates to generate carbon/Si core–shell structures. Kumta et al. [9] reported synthesis of vertically aligned Si/carbon nanotube arrays directly on Inconel

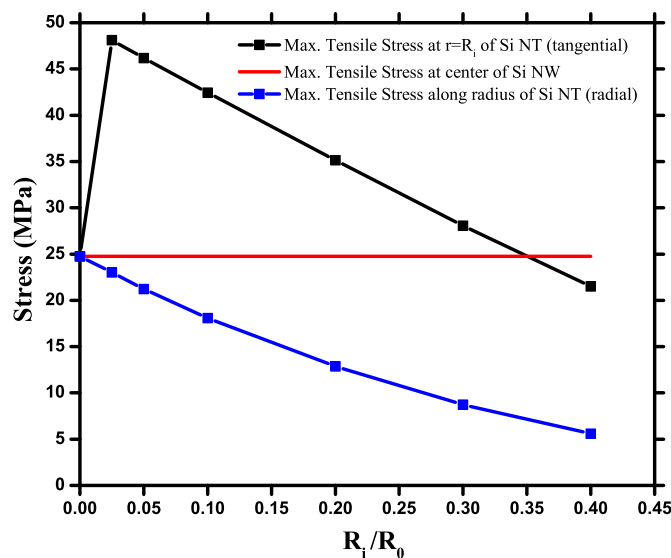


Fig. 9. Comparison of maximum tensile stresses of Si NT with increasing R_i/R_0 ratios. The thick red line represents the maximum tensile stress at the center of Si NW ($R_i/R_0 = 0$). (For interpretation of the references to color in this figure legend, the reader is referred to the web version of this article.)

metal current collector, using a two-step chemical vapor deposition process. Justin et al. [11] reported synthesis of smooth and conformal thin films on various multi-walled carbon nanotube using radio frequency plasma enhanced chemical vapor deposition. For the simulations considered here, single-walled carbon nanotube (SWCNT) and multi-walled carbon nanotube (MWCNT) structures were chosen as the materials for core, and amorphous Si as the shell material. The Young's modulus of SWCNT and MWCNT are 200 and 30 GPa respectively [13]. The SWCNT(MWCNT)/Si core–shell structure has an outer radius of 50 nm with a SWCNT (MWCNT) core of radius $R_{int} = 1/10R_0$, i.e., 5 nm. Fig. 10 plots the radial stress profiles for SWCNT/Si and MWCNT/Si structures at times of 1, 10, and 100 s, respectively. For both these structures, the radial stresses are always maximum at the center extending up to CNT/Si interface. This is similar to Si NW structure, where the maximum radial stress always occurs at the center, however this maximum value extends up to the CNT/Si interface because of the constant stresses within the core (Appendix I). The maximum observed radial stress at the CNT/Si interface extends into the core, and does not vary spatially within the core. Since the core does not insert lithium, therefore under such circumstances, the radial stresses should remain constant based on the force balance equations (see Appendix I). Furthermore, the radial stresses in the core and the shell, increases sharply with time which is quite different in behavior from other nanostructures, Si NW and Si NT. This is due to the discontinuity of concentration variable at the interface combined with the absence of free surface. The magnitude of radial stresses are larger for SWCNT/Si structure compared to the MWCNT/Si structure due to the lower magnitude of Young's modulus of the MWCNT compared to SWCNT. The absence of chemical strain and the high value of elastic moduli, resists movement of the interface. The interface does not move up to first 100 s of lithiation.

Fig. 11 shows maximum radial stress evolution of SWCNT(MWCNT)/Si structures with time and compares them to Si NW. The maximum radial stress magnitudes for both Si shell carbon core structures are much higher compared to Si NW. It is to be noted that at very short times (<2 s), MWCNT/Si maximum radial stress is lower than Si NW maximum stress. This is because at those short times, chemical strain component is almost insignificant. So the strains are mainly elastic strains. Since MWCNT has the lowest elastic modulus compared to other materials considered here,

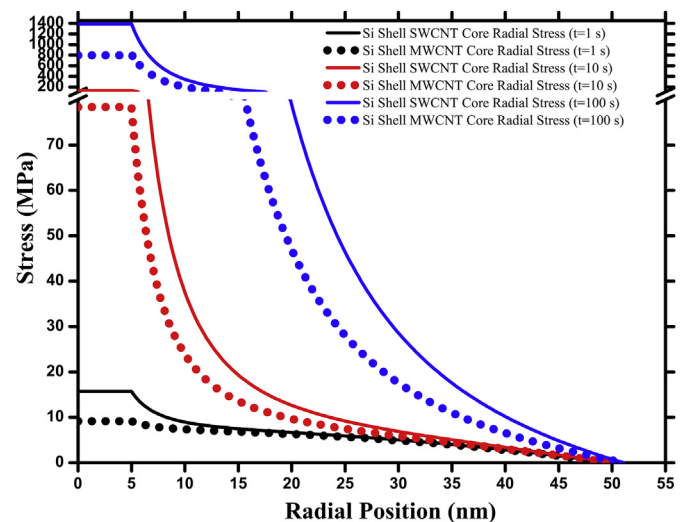


Fig. 10. Comparison of radial stress profiles for Si SWCNT and Si MWCNT at various times $t = 1, 10$ and 100 s.

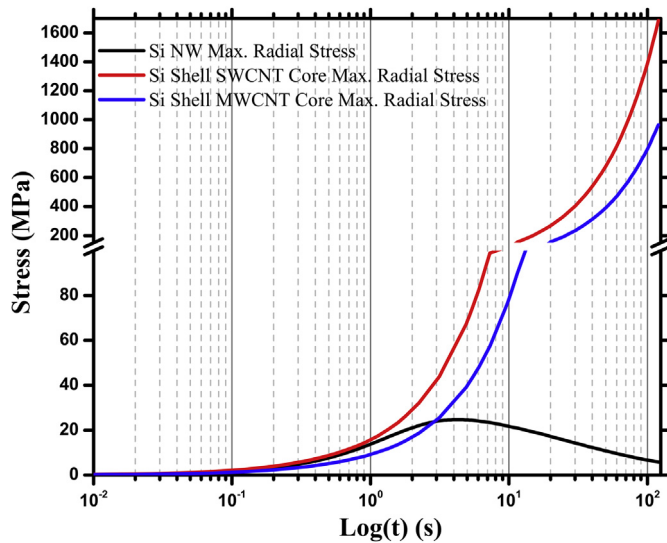


Fig. 11. Comparison of maximum radial stress profile for Si NW and core radial stress profiles for Si SWCNT and Si MWCNT with time.

therefore it generates lower stress. Fig. 12 compares the tangential stress profiles for SWCNT/Si and MWCNT/Si structures at times of 1 and 10 s. For both the core shell structures, tangential stresses are tensile inside the core which increase with time while at outer surface they are fully compressive. This behavior is similar to Si NW structure. Much higher stresses are observed as a result of the non-insertion core. The tangential stress for both structures become discontinuous at the core–shell interface and turns more compressive with time. The tangential stresses for the MWCNT/Si structure are less compared to the SWCNT/Si structure. For example, at $t = 100$ s, the maximum tangential stress for the MWCNT/Si structure has a magnitude of 612 MPa compared to 1024 MPa for the SWCNT/Si structure.

Fig. 13 shows a summary plot comparing the radial stress profiles for different structures discussed earlier. The plots suggest that core shell structures with non-insertion core clearly develop higher stresses compared to Si NT and Si NW. On the other hand, Si NT structure generates lower stresses than Si NW and CNT/Si core–

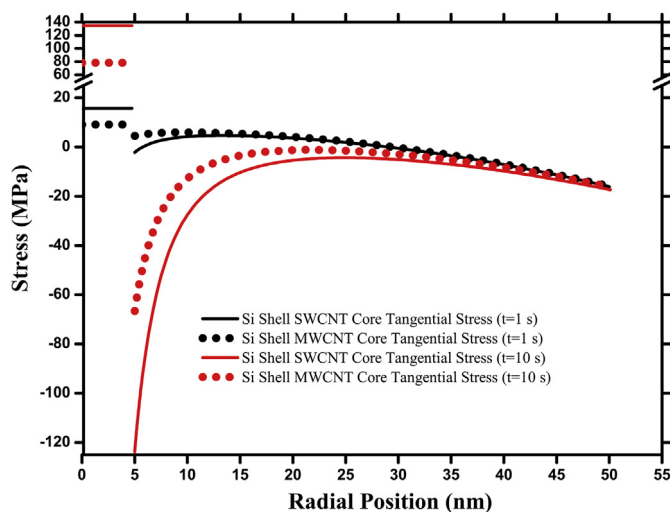


Fig. 12. Comparison of tangential stress profiles for Si SWCNT and Si MWCNT at times $t = 1$ and 10 s.

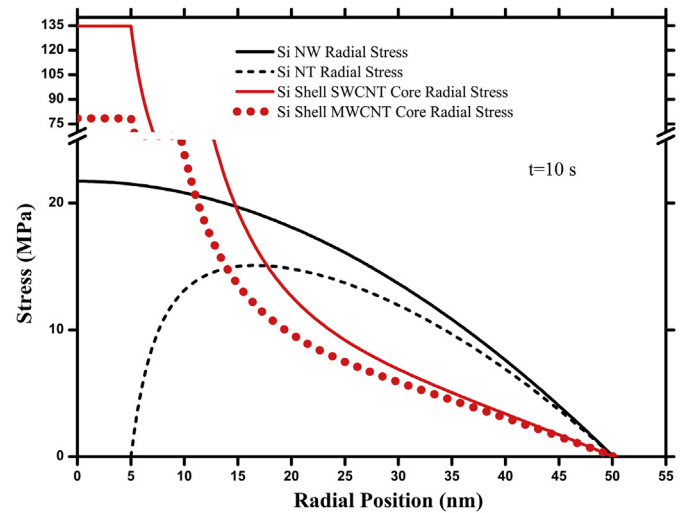


Fig. 13. Comparison of radial stress profiles for Si NW, Si NT, Si SWCNT and Si MWCNT at times $t = 10$ s.

shell structures (for similar current densities) which could be a preferred structure for practical use. Core–shell structures with substantial lithium insertion cores will behave differently from the structures considered here because of the continuous lithium concentration gradients across the interfaces. This will be a subject of future work.

5. Conclusion

A 1-d axisymmetric plane strain stress model coupled with pressure induced diffusion was developed to analyze stress distribution during lithium insertion in different silicon based nanostructures (Si NW, Si NT, Si shell carbon core). The results from simulation of lithiation of Si NW using the 1-d model are compared to the results from the 2-d model presented in part I of the paper. The two models agree very well at short times, however tend to deviate slightly at longer times. Also, the modeling results infer that Si NT could be a better structure in terms of mechanical stability as it generates lower stresses compared to Si NW and CNT/Si core–shell structures. Furthermore, core–shell structures (SWCNT/Si and MWCNT/Si) exhibit very high stresses at the core–shell interface.

Acknowledgments

Applied Materials Inc. assisted in meeting the publication costs of this article.

Appendix I

The radial and tangential stresses inside the core for a Si shell carbon core structure, are both constant across radius. Moreover, in the core the radial and tangential stresses are equal. In this section, a mathematical approach is explained to verify this behavior. In the carbon core, Eq. (5) is valid. In addition, two other assumptions are made here:

- As only elastic strains exist in non-insertion carbon core, and the deformation is very small, linear theory of elasticity is assumed to hold good.
- Movement of core–shell interface is neglected.

Replacing the stress terms in Eq. (5) with respect to displacement u we get

$$r^2 \frac{d^2 u}{dr^2} + r \frac{du}{dr} - u = 0 \quad (17)$$

The general solution of this kind of ODE is $u = c_1 r + c_2/r$ where c_1 and c_2 are constants of integration. Applying symmetry boundary condition at $r = 0$, the final solution is $u = c_1 r$. Plugging this solution back to the radial and tangential stress expressions, it can be proved that σ_{rr} and $\sigma_{\theta\theta}$ are constant and equal to each other in the core.

Appendix II

For development of both 2-d and 1-d model, we split the total strain ϵ_T into chemical and elastic components i.e., ϵ_{ch} and ϵ_{el} . This methodology is extensively reported in literature [14–18]. Christensen et al. [19] reports a slightly different technique, where in the total stress is split into an elastic component and thermodynamic pressure. The thermodynamic pressure p is solved as a separate variable. The author claims that this approach is more general as p is not restricted to being just a function of stress tensor. In this work, the thermodynamic pressure p is assumed to be equivalent to the mean normal pressure which is function of stress tensor as discussed earlier in Part I. To understand the difference between either of the approaches, we developed the 1-d axisymmetric model based on the procedure of splitting the stress, and compared to the alternate approach of splitting the strain. Fig. 14 shows the comparisons of maximum radial and tangential stress profiles with time of Si NW of radius 50 nm from both the 1-d models developed following the stress and strain splitting procedures. Both approaches show very good qualitative comparison – maximum radial stress at center and maximum tangential stress variation at outer surface is predicted by either approach. At short times, the radial stresses predicted by the stress splitting method is slightly higher than the strain splitting method, while the tangential stresses are quantitatively very close. The maxima (with time) predicted for both radial and tangential stresses using the strain splitting approach is larger compared to the stress splitting approach. Moreover, the occurrence of the peak stresses is also shifted to the right for the strain splitting method. The pressure gradient in the Li flux equation is a dominating factor controlling

lithium insertion which affects the thermodynamic pressure and in turn the stresses. This effect becomes prominent when the Li concentration gradients are high at shorter times which explains the deviation between the two approaches. At prolonged times, the concentration gradients become more uniform which prevents the profiles from diverging at longer times.

Nomenclature

c_T	total concentration of species, mol m ⁻³
N	flux of species S, or LiS, mol/m ² s
x_{LiS}	mole fraction of species, LiS
Δz	insertion coefficient of Li in Li _{Δz} Si _{1/Δz}
Δx	maximum number of moles of Li that can reversibly alloy per mole of Si
t	time, s
r	radial co-ordinate, m
θ	tangential co-ordinate, deg
z	axial co-ordinates, m
$D_{LiS,S}$	binary diffusion coefficient of Li in LiS, m ² s ⁻¹
α_{LiS}	thermodynamic factor
M_{LiS}	molar mass of species, LiS, g mol ⁻¹
F	Faraday's constant, C g ⁻¹ equiv
R	universal gas constant, J mol ⁻¹ K
T	temperature, K
s_i	stoichiometric coefficient
\bar{V}_{LiS}	partial molar volume of species, LiS, m ³ mol ⁻¹
ρ	density of Li _z Si _{1/Δz} , g m ⁻³
p	thermodynamic pressure, N m ⁻²
\mathbf{u}	displacement vector field
u	displacement in r co-ordinate, m
n	unit outward normal vector, m
i_{app}	current density related to the outer surface area of the nanostructures, A m ⁻²
τ	stress tensor matrix
σ	stress components of the stress tensor matrix, N m ⁻²
ϵ	strain tensor matrix
ϵ	strain components of the strain tensor matrix, N m ⁻²
λ	lame constant given by $E\nu/(1+\nu)$, N m ⁻²
μ	Lame constant given by $E/2(1+\nu)(1-2\nu)$, N m ⁻²
E	Young's modulus, N m ⁻²
ν	Poisson's ratio

Subscripts

LiS	lithiated host
S	unoccupied host
T	total
max	maximum

References

- [1] C.K. Chan, H. Peng, G. Liu, K. McIlwrath, X.F. Zhang, R.A. Huggins, Y. Cui, Nat. Nano 3 (1) (2008) 31–35.
- [2] C.K. Chan, R.N. Patel, M.J. O'Connell, B.A. Korgel, Y. Cui, ACS Nano 4 (3) (2010) 1443–1450.
- [3] L.F. Cui, R. Ruffo, C.K. Chan, H.L. Peng, Y. Cui, Nano Lett. 9 (1) (2009) 491–495.
- [4] T. Song, J.L. Xia, J.H. Lee, D.H. Lee, M.S. Kwon, J.M. Choi, J. Wu, S.K. Doo, H. Chang, W. Il Park, D.S. Zang, H. Kim, Y.G. Huang, K.C. Hwang, J.A. Rogers, U. Paik, Nano Lett. 10 (5) (2010) 1710–1716.
- [5] M.-H. Park, M.G. Kim, J. Joo, K. Kim, J. Kim, S. Ahn, Y. Cui, J. Cho, Nano Lett. 9 (11) (2009) 3844–3847.
- [6] A. Magasinski, P. Dixon, B. Hertzberg, A. Kvit, J. Ayala, G. Yushin, Nat. Mater. 9 (4) (2010) 353–358.
- [7] Y. Yao, M.T. McDowell, I. Ryu, H. Wu, N. Liu, L. Hu, W.D. Nix, Y. Cui, Nano Lett. 11 (7) (2011) 2949–2954.
- [8] N. Liu, H. Wu, M.T. McDowell, Y. Yao, C. Wang, Y. Cui, Nano Lett. 12 (6) (2012) 3315–3321.
- [9] W. Wang, R. Epur, P.N. Kumta, Electrochem. Commun. 13 (5) (2011) 429–432.
- [10] R. Krishnan, T.-M. Lu, N. Koratkar, Nano Lett. 11 (2) (2011) 377–384.

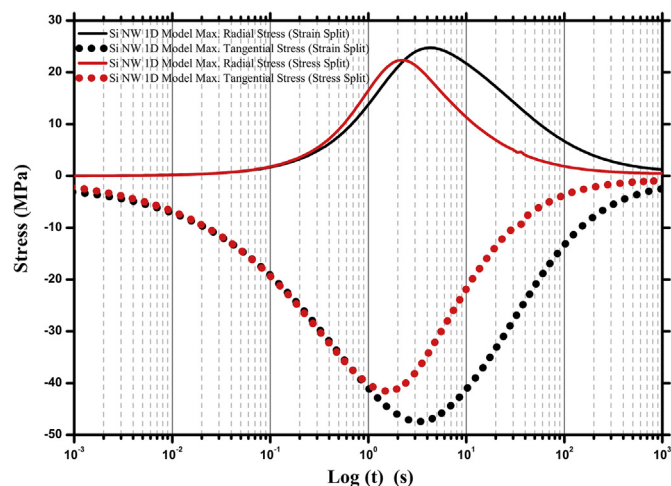


Fig. 14. Comparison of maximum radial and tangential stress profiles of Si NW from 1-d models (strain and stress splitting).

- [11] J.J. Nguyen, K. Evanoff, W.J. Ready, *Thin Solid Films* 519 (13) (2011) 4144–4147.
- [12] L.-F. Cui, Y. Yang, C.-M. Hsu, Y. Cui, *Nano Lett.* 9 (9) (2009) 3370–3374.
- [13] I. Palaci, S. Fedrigo, H. Brune, C. Klinke, M. Chen, E. Riedo, *Phys. Rev. Lett.* 94 (17) (2005) 175502–1–175502–4.
- [14] M.W. Verbrugge, Y.-T. Cheng, *J. Electrochem. Soc.* 156 (11) (2009) A927–A937.
- [15] Y.T. Cheng, M.W. Verbrugge, *J. Power Sources* 190 (2) (2009) 453–460.
- [16] R. Deshpande, Y.-T. Cheng, M.W. Verbrugge, *J. Power Sources* 195 (15) (2010) 5081–5088.
- [17] X.C. Zhang, A.M. Sastry, W. Shyy, *J. Electrochem. Soc.* 155 (7) (2008) A542–A552.
- [18] X.C. Zhang, W. Shyy, A.M. Sastry, *J. Electrochem. Soc.* 154 (10) (2007) A910–A916.
- [19] J. Christensen, J. Newman, *J. Solid State Electrochem.* 10 (5) (2006) 293–319.
- [20] N. Ding, J. Xu, Y.X. Yao, G. Wegner, X. Fang, C.H. Chen, I. Lieberwirth, *Solid State Ionics* 180 (2–3) (2009) 222–225.
- [21] B. Hertzberg, J. Benson, G. Yushin, *Electrochem. Commun.* 13 (8) (2011) 818–821.